ACS APPLIED MATERIALS & INTERFACES

Research Article

www.acsami.org

Porous Graphitic Carbon Loading Ultra High Sulfur as High-Performance Cathode of Rechargeable Lithium−Sulfur Batteries

Gui-Liang Xu, Yue-Feng Xu, Jun-Chuan Fang, Xin-Xing Peng, Fang Fu, Ling Huang, Jun-Tao Li, and Shi-Gang Sun*

State Key Laboratory of Physical Chemistry of Solid Surfaces, Department of Chemistry, College of Chemistry and Chemical Engineering, Xiamen University, Xiamen 361005, China

Supporting Information

ABSTRACT: Porous graphitic carbon of high specific surface area of 1416 m^2 g^{-1} and high pore volume of 1.11 cm^3 g^{-1} is prepared by using commercial $CaCO_3$ nanoparticles as template and sucrose as carbon source followed by 1200 °C high-temperature calcination. Sulfur/porous graphitic carbon composites with ultra high sulfur loading of 88.9 wt % (88.9%S/PC) and lower sulfur loading of 60.8 wt % (60.8%S/PC) are both synthesized by a simple melt-diffusion strategy, and served as cathode of rechargeable lithium−sulfur batteries. In comparison with the 60.8%S/PC, the 88.9%S/PC exhibits higher overall discharge capacity of 649.4 mAh $g^{-1}_{(S-C)}$, higher capacity retention of 84.6% and better coulombic efficiency of 97.4% after 50 cycles at a rate of 0.1C, which benefits from its remarkable specific capacity with such a high sulfur loading. Moreover, by using BP2000 to replace the conventional acetylene black conductive agent, the 88.9% S/PC can further improve its overall discharge capacity and high rate property. At a high rate of 4C, it can still deliver an overall discharge capacity of 387.2 mAh $g^{-1}_{(S-C)}$. The porous structure, high specific surface area, high pore volume and high electronic conductivity that is originated from increased graphitization of the porous graphitic carbon can provide stable electronic and ionic transfer channel for sulfur/porous graphitic carbon composite with ultra high sulfur loading, and are ascribed to the excellent electrochemical performance of the 88.9%S/PC.

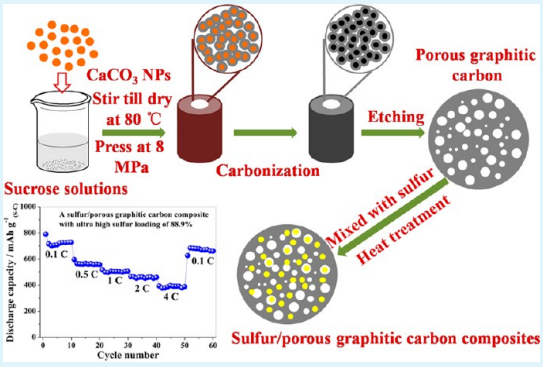

KEYWORDS: *porous graphitic carbon, sulfur/carbon composite, high sulfur loading, ovreall capacity, BP2000, Li−S batteries*

1. INTRODUCTION

Rechargeable lithium−sulfur (Li−S) batteries have been considered as one of the most promising candidates for powering electric vehicles (EVs) due to its high theoretical specific energy (2600 Wh/kg), which is 3−5 times higher than that of current Li-ion batteries based on intercalation chemistry.[1] Nevertheless, there remain several challenges that inhibit Li−S batteries for practical application in EVs. The first challenge consists in the electrical insulating nature of elemental sulfur (5×10^{-30} S cm^{-1} at 25 °C) and its discharge products, leading to low utilization of active material in the cathode owing to the poor electrochemical contact with sulfur.[2] The second challenge lies in the intrinsic polysulfide shuttle, which is attributed to the high solubility of lithium polysulfides (Li_2S_x, $2 < x \leq 8$) in the commonly used ether-based electrolytes, resulting in poor cycleability, high current leakage, and poor charge/discharge efficiency.[3,4] Moreover, a fraction of the polysulfides is transformed into Li_2S_2 and/or Li_2S and then deposited on the surface of lithium anode, forming a thick layer during repeated cycling. As a result, a progressive loss of active material, a degradation of electrode structure, and an increase in internal cell impedance have occurred.

In the past decades, extensive efforts have been devoted to prevent polysulfide dissolution and shuttling. One approach is the protection of lithium anode or the restraining of the ionic mobility of the polysulfide anions, which would both lower the transport of lithium ions and further decrease the power density.[5−7] The other approach is to use electrolyte additives ($LiNO_3$) to mitigate the solubility problem of polysulfides in electrolyte, which can form a stable passivation film on the surface of lithium anode.[8,9] Such film can protect lithium anode from chemical reaction with the polysulfides, and also prevent the polysulfides from electrochemical reduction on the Li anode surface, and hence greatly increase the cycling efficiency.

On the other hand, extensive studies have been conducted to the construction of sulfur/carbon composites as a result of the unique advantages of carbonaceous materials, such as high electronic conductivity, good accessibility of liquid electrolytes to active material and superior affinity for sulfur and polysulfides within the framework. A breakthrough progress have been made by Nazar and coworkers by employing a nanostructured sulfur/mesoporous graphitic carbon cathode that could overcome those problems to a large extent, and exhibit stable, highly reversible capacities.[1] Various carbona-

Received: July 22, 2013
Accepted: October 3, 2013
Published: October 3, 2013

ceous materials such as conductive polymer,[10−14] carbon nanotubes,[15−19] carbon spheres,[20−22] porous carbon,[2,23] carbon nanofibers,[24−26] graphene oxide sheets[3,27−29] and graphene sheets[28,30−33] have been investigated as conductive carbon matrix for sulfur cathodes, and demonstrated improved cycleability and rate capability in comparison with pristine sulfur. We have recently reported sulfur/reduced graphene oxide (S/rGO) sheets composites,[3] sulfur/ordered mesoporous carbon (S/OMC),[4] and sulfur/expanded graphite (S/EG).[34] By systematic variation and optimization of the sulfur loading, we find that S/(OMC, EG and rGO) composites with sulfur loadings of around 60 wt % show the highest specific capacity around 800−900 mAh $g^{-1}_{(s)}$ after 80 cycles at a rate of 0.1C amongst the S/(OMC, EG and rGO) composites with different sulfur loadings.

The third challenge is the sulfur loading in the sulfur/carbon composites, which greatly affect the energy density of Li−S batteries in practical application. As most carbon can only offer little capacity in the tested voltage range (1.5−3.0 V vs. Li/Li^+) for sulfur electrodes, the overall capacity of sulfur/carbon composites equals to the sulfur loading times the specific capacity. In order to increase the energy density of Li−S batteries, one way is to improve the specific capacities of sulfur/carbon composites, which has been extensively done by fabrication of sulfur/carbon composites with appropriate sulfur loadings (30−70 wt %). Another way is to increase the sulfur loading in the sulfur/carbon composites. However, owing to the insulating nature of sulfur, high sulfur loadings in the sulfur/carbon composites will decrease the electrical contact with sulfur, leading to poor electrochemical properties. In our previous studies,[3,4,34] we find that sulfur/carbon composites with sulfur loading over 70 wt % exhibit low specific capacities and rapid capacity fading, resulting in low overall capacities. Nazar et al. have reported a graphene/sulfur composite with a sulfur fraction as high as 87 wt % by a heterogeneous nucleation method, which can deliver a high overall discharge capacity.[35] They attribute their promising properties to the high conductive shrink-wrap of graphene for electron transport. Li and coworkers have recently prepared a sulfur/peapod-like carbon composite with a high sulfur loading up to 84 wt %. Despite the high specific surface area (922 $m^2\ g^{-1}$) and large pore volume (4.69 $cm^3\ g^{-1}$) of the peapod-like carbon that can encapsulate high content sulfur, the overall discharge capacity of the sulfur/peapod-like carbon composite has decayed below 400 mAh $g^{-1}_{(S-C)}$ after 50 cycles at a rate of 0.2 C.[36] These results indicate that the electronic conductivity of carbonaceous material may be the key factor influencing the electrochemical properties of sulfur/carbon composites with ultra high sulfur loadings. As a consequence, it is a great challenge to prepare carbonaceous materials with high electronic conductivity for developing high specific energy Li−S batteries.

In the current study, we have developed a facile route to prepare a porous graphitic carbon by using commercial $CaCO_3$ nanoparticles as template and sucrose as carbon source followed by 1200 °C high temperature calcination. The obtained porous graphitic carbon possesses a high specific surface area up to 1416 $m^2\ g^{-1}$, a high pore volume of 1.11 $cm^3\ g^{-1}$ and a high electronic conductivity that is originated from increased graphitization. Sulfur/porous graphitic carbon composite with ultra high sulfur loading of 88.9 wt % (88.9% S/PC) has been obtained by a simple melt-diffusion strategy. The 88.9%S/PC served as cathode for Li−S batteries could deliver an overall discharge capacity of 649.4 mAh $g^{-1}_{(S-C)}$, high capacity retention of 84.6% and a superior coulombic efficiency of 97.4% after 50 cycles at 0.1 C. Moreover, by using BP2000 to replace conventional acetylene black as conductive agent, the overall discharge capacity and high rate property of 88.9%S/PC has been further improved. An overall discharge capacity of 448.6 mAh $g^{-1}_{(S-C)}$ after 200 cycles at 0.5 C and 387.2 mAh $g^{-1}_{(S-C)}$ at a high rate of 4 C is achieved. The excellent electrochemical properties of the 88.9%S/PC are attributed to the porous structure, high specific surface area, high pore volume and high electronic conductivity of the porous graphitic carbon, which can provide stable electronic and ionic transfer channels for the sulfur/porous graphitic carbon composite with ultra high sulfur loading.

2. EXPERIMENTAL SECTION

2.1. Materials Synthesis. In a typical synthesis of porous graphitic carbon, commercial $CaCO_3$ nanoparticles (ca. 40 nm) and sucrose were served as template and carbon source, respectively. Five grams of sucrose was dissolved into 40 mL of deionized water; 10 g of $CaCO_3$ nanoparticles were then added into the sucrose solution under continuous stirring. The mixture was stirred until dry at 80 °C water bath. The obtained white powder was collected and pressed at 8 MPa by a home-made mold. Then it was carbonized at 1200 °C for 2 h under an argon atmosphere with a heating rate of 5 °C min^{-1}. After removal of the $CaCO_3$ template by 30 wt % HCl, porous graphitic carbon was obtained. The sulfur/porous graphitic carbon composites were then prepared, in a sealed Teflon container at 155 °C for 12 h, by simply heating the mixture of sublimed sulfur and porous graphitic carbon at accurate weight ratios of X:$(1 - X)$, denoted as X%S/PC, where X represented the weight percentage of sulfur.

2.2. Materials Characterization. The morphologies and structures of sublimed sulfur, the as-prepared porous graphitic carbon and sulfur/porous graphitic carbon composites were characterized by field emission scanning electron microcopy (HITACHI S-4800) and/or transmission electron microcopy (JEM-1400, F30). Powder X-ray diffraction (XRD, Philips X'pert Pro Super X-ray diffractometer and Rigaku Ultima IV, Cu Kα radiation) was used for phase analyses. The specific surface areas and pore volumes of porous graphitic carbon, sublimed sulfur and sulfur/porous graphitic carbon composites were measured by the Brunauer−Emmett−Teller (BET) method using nitrogen adsorption and desorption isotherms on a Tristar3000 system. Pore size distribution plot was obtained by Barrett−Joyner−Halenda (BJH) method. Thermogravimetric analyses (TGA) were carried out under N_2 atmosphere on a TG_209F1 instrument to detect the sulfur loadings in the sulfur/porous graphitic carbon composites. The temperature range was from room temperature to 600 °C, and the temperature rising rate was 10 °C min^{-1}. FT-IR analysis was carried out using pressed KBr disks in the range 4000−400 cm^{-1} using a Nicolet 330 spectrometer.

2.3. Electrochemical Measurements. The cathode were prepared by spreading a mixture of 70 wt % sulfur/porous graphitic carbon composites or sublimed sulfur, 20 wt % acetylene black (or BP2000) and 10 wt % LA132 binder onto an aluminum foil current collector. The electrodes using acetylene black as conductive agent were denoted as Y-AB, and the electrodes using BP2000 as conductive agent were denoted as Y-BP2000, where Y represented the sulfur/porous graphitic carbon composites or sublimed sulfur electrodes. The as-prepared electrode sheets were dried at 55 °C for 24 h in a vacuum oven and then pressed under 10 MPa. The electrochemical measurements were carried out with 2025 coin cells assembled in an argon-filled glove box with lithium metal as reference and counter electrode. The electrodes were separated by a separator (Celgard 2400). Electrolyte used in the cell was 1.0 M lithium bis-trifluoromethanesulfonylimide in a mixture of 1,3-dioxolane (DOL) and dimethoxyethane (DME) (1:1 by volume) with 0.2 M $LiNO_3$ additive. The rate set for cell tests was referenced to the mass of sulfur active material in the cathode, and 1C equaled to 1675 mA g^{-1}. The specific capacity calculated based on the mass of sulfur active material

was denoted as mAh $g^{-1}_{(S)}$, whereas the overall capacity calculated based on the mass of total sulfur/porous graphitic carbon composite was denoted as mAh $g^{-1}_{(S-C)}$. The charge/discharge voltage range was 1.5−3.0 V vs. Li/Li^+. Cyclic voltammetry (CV) of the sulfur/porous graphitic carbon composites, sublimed sulfur and porous graphitic carbon electrodes were tested at an electrochemistry working station CHI 660C (CH Instruments, shanghai) with a potential scan rate of 0.1 mV s^{-1}. Electrochemical impedance spectroscopy (EIS) measurements were carried out on electrochemical workstation (PARSTAT 2263, Princeton Applied Research, USA) with a frequency range from 100 kHz to 1 Hz.

3. RESULTS AND DISCUSSION

Scheme 1 illustrates the formation procedure of porous graphitic carbon and sulfur/porous graphitic carbon composites. $CaCO_3$ nanoparticles and sucrose are served as template and carbon source, respectively. During the stirring process, sucrose is coated on the surface of $CaCO_3$ nanoparticles. After stirring till dry, the mixture is pressed into a monolith by a home-made mold. The sucrose is decomposed into carbon, and the $CaCO_3$ is reduced to CaO and CO_2 during carbonization at a high temperature of 1200 °C under argon atmosphere. After removal of CaO by 30 wt % HCl, porous graphitic carbon is obtained. The formation of the porous structure could be ascribed to the release of CO_2 and the removal of CaO. Sulfur/porous graphitic carbon composites with different sulfur loadings are then synthesized by a simple melt-diffusion strategy. The binding between sulfur and porous graphitic carbon by this method is very strong, and it does not produce hazardous H_2S gas as the heterogeneous nucleation method does.[37] In a word, we demonstrate a facile route to synthesize porous graphitic carbon and sulfur/porous graphitic carbon composites.

Scheme 1. Synthesis Route for Porous Graphitic Carbon and Sulfur/Porous Graphitic Carbon Composite

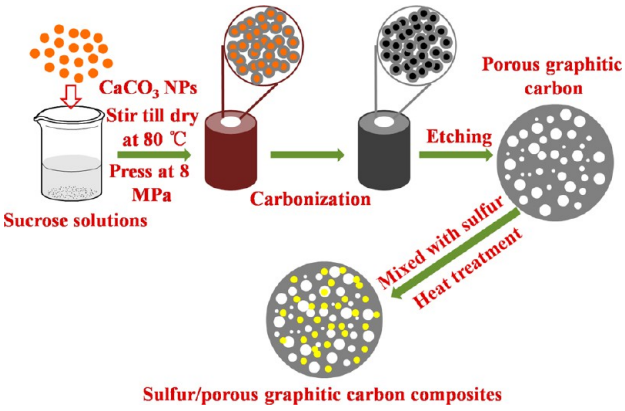

Images a and b in Figure 1 illustrate the low- and high-magnification SEM images of the as-prepared porous graphitic carbon, respectively. As shown, the porous graphitic carbon possesses a porous structure with a large amount of nanopores. Figure 1c demonstrates typical nitrogen adsorption/desorption isotherms of the porous graphitic carbon at 77 K. It presents a type IV isotherm according to the IUPAC classification, indicating the characteristic mesoporous structure of porous graphitic carbon. It is further confirmed by the pore size distribution (Figure 1d). As shown, the pore size distribution of porous graphitic carbon is ranging from 0.5 to ca. 50 nm, and mainly distributed at the pore size less than ca. 2 nm. According to the IUPAC, mesopores are range from 2 to 50 nm and

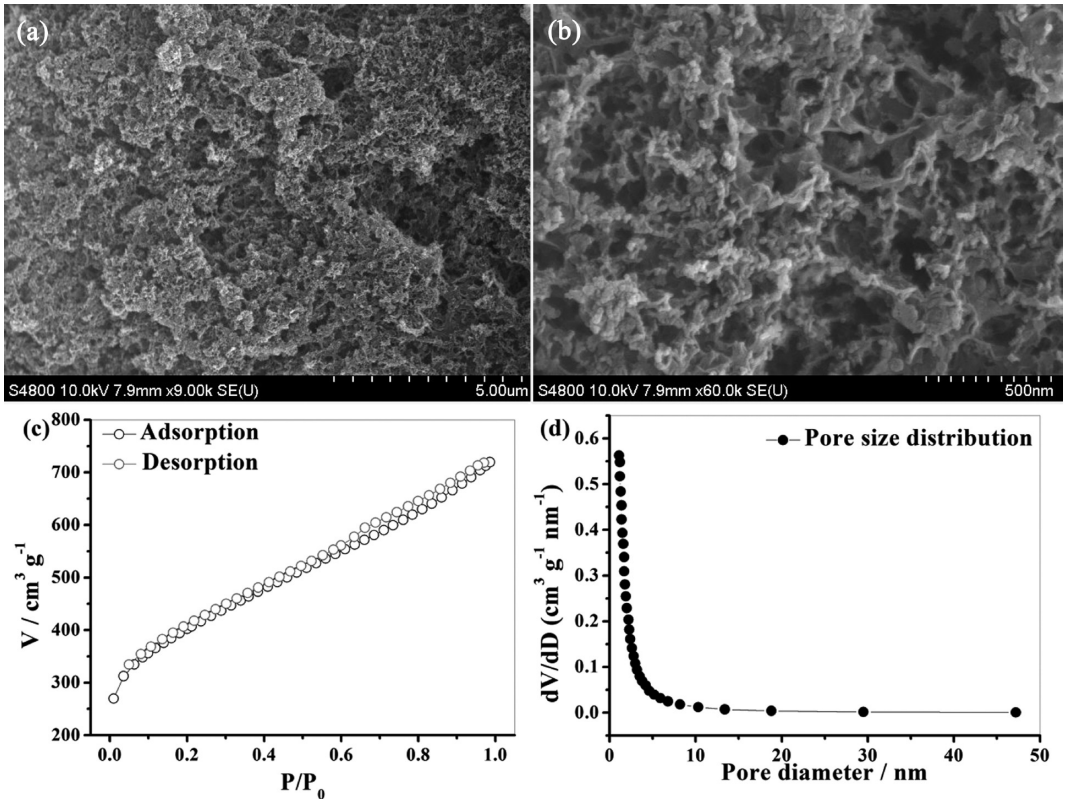

Figure 1. (a) Low- and (b) high-magnification SEM images of porous graphitic carbon; (c) N_2 adsorption/desorption isotherm curve and (d) pore size distribution of porous graphitic carbon.

micropores are less than 2 nm. Therefore, the pore volume of porous graphitic carbon is mainly attributed by the micropores. The specific surface area and the pore volume of porous graphitic carbon are determined 1416 $m^2 g^{-1}$ and 1.11 $cm^3 g^{-1}$, respectively, which are beneficial for the dispersion of sulfur nanoparticles and access of electrolyte throughout the porous structure of porous graphitic carbon. TGA analyses (Figure 2)

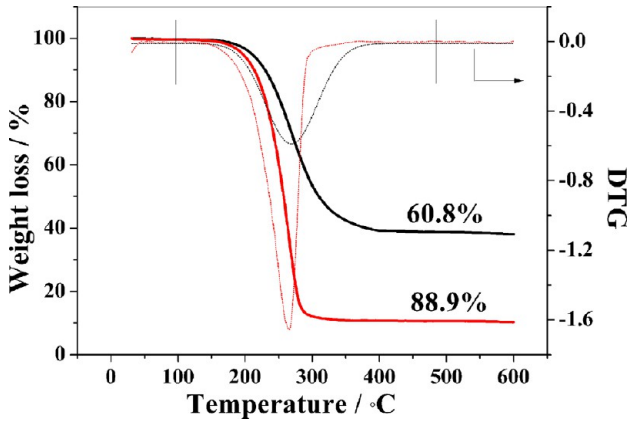

Figure 2. TGA and DTG curve of 60.8%S/PC and 88.9%S/PC under a N_2 atmosphere.

of sulfur/porous graphitic carbon composites are conducted in order to determine the sulfur loadings. There are major mass losses from 200 to 500 °C due to the evaporation of sulfur from the sulfur/porous graphitic carbon composites. The sulfur loadings are determined based on the difference of weight losses between 100 °C and 500 °C, which are measured to be 60.8 and 88.9 wt %, respectively. The sulfur/porous graphitic carbon composites are therefore denoted correspondingly as 60.8%S/PC and 88.9%S/PC. To the best of our knowledge, such a high sulfur loading of 88.9 wt % in the sulfur/carbon composites has been rarely reported.

X-ray diffraction (XRD) patterns of porous graphitic carbon, 60.8%S/PC and 88.9%S/PC composites are compared in Figure 3. In addition to two broad peaks at 24.0 and 43.8°, three crystalline peaks that correspond to the reflections of graphitic planes (002), (100), and (101) can be observed in the XRD pattern of porous graphitic carbon (Figure 3a).[38] The presence of these peaks is attributed to the 1200 °C high temperature calcination during carbonization, implying an increased graphitization of the as-prepared porous graphitic carbon than conventional amorphous carbon. It is commonly accepted that the higher degree of graphitization, the higher electronic conductivity. Therefore, the as-prepared porous graphitic carbon could exhibit a high electronic conductivity by high temperature calcination. For the 60.8%S/PC (Figure 3b), only the diffraction of porous graphitic carbon is observed, no diffraction peaks of sulfur can be identified, indicating that the crystalline sulfur has been converted into amorphous sulfur and there are no big sulfur nanoparticles in the 60.8%S/PC. However, in the case of 88.9%S/PC (Figure 3b), it displays almost the characteristic of sublimed sulfur, indicating the presence of crystalline sulfur and large sulfur particles on the surface of porous graphitic carbon. This is similar to the result of XRD patterns of sulfur/carbon composites with high sulfur loading.[3] From the SEM image of 88.9%S/PC in Figure S1a in the Supporting Information, we can observe part of big sulfur particles on the surface of porous graphitic carbon, which should be responsible for the strong sulfur diffraction peaks in the XRD pattern of 88.9%S/PC. While from the SEM image of sublimed sulfur (see Figure S1b in the Supporting Information), we can see lots of large aggregated sulfur particles. We have also measured the BET of 60.8%S/PC and 88.9%S/PC as well as sublimed sulfur. Their N_2 adsorption and desorption isotherm curves are compared in Figure S2 in the Supporting Information. As illustrated, after encapsulation of sulfur nanoparticles into the porous graphitic carbon matrix, the specific surface areas and pore volumes of 60.8%S/PC and 88.9%S/PC have both significantly decreased. In the case of 60.8%S/PC, because of lower sulfur loading, it can still possess a specific surface area of 13.7 $m^2 g^{-1}$ and a pore volume of 0.15 $cm^3 g^{-1}$. However, for the 88.9%S/PC, because of the ultra high sulfur loading in the porous graphitic carbon, its specific surface area and pore volume are very close to those of sublimed sulfur, and become very low.

The morphologies of sulfur/porous graphitic carbon composites are very important to understand the dispersion of sulfur nanoparticles in the porous graphitic carbon matrix. The TEM images of porous graphitic carbon, 60.8%S/PC and 88.9%S/PC are shown in Figure 4. As shown in panels a and b in Figure 4, the porous graphitic carbon exhibits a porous structure with nanopores ranging from several to tens of nanometers. After sulfur encapsulation, as shown in panels c and d in Figure 4, sulfur nanoparticles are uniformly dispersed into the mesopores of porous graphitic carbon in the case of

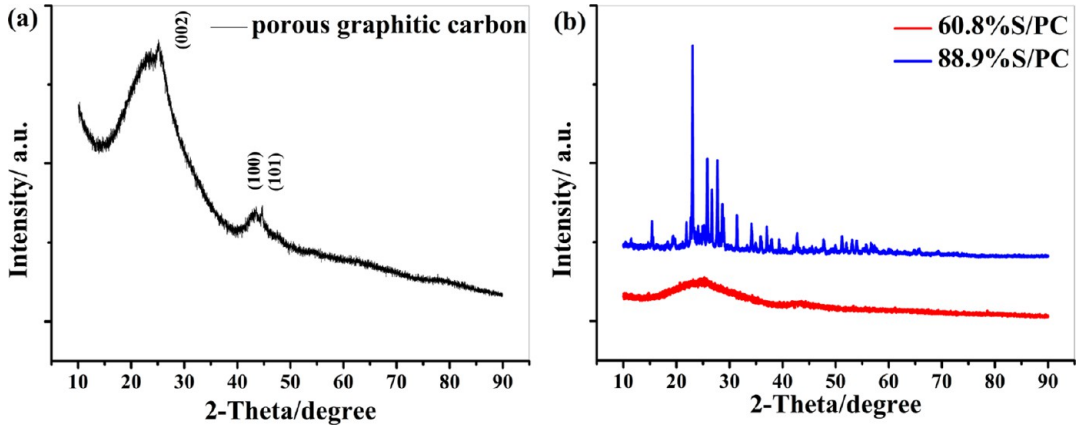

Figure 3. XRD patterns of (a) porous graphitic carbon and (b) sulfur/porous graphitic carbon composites.

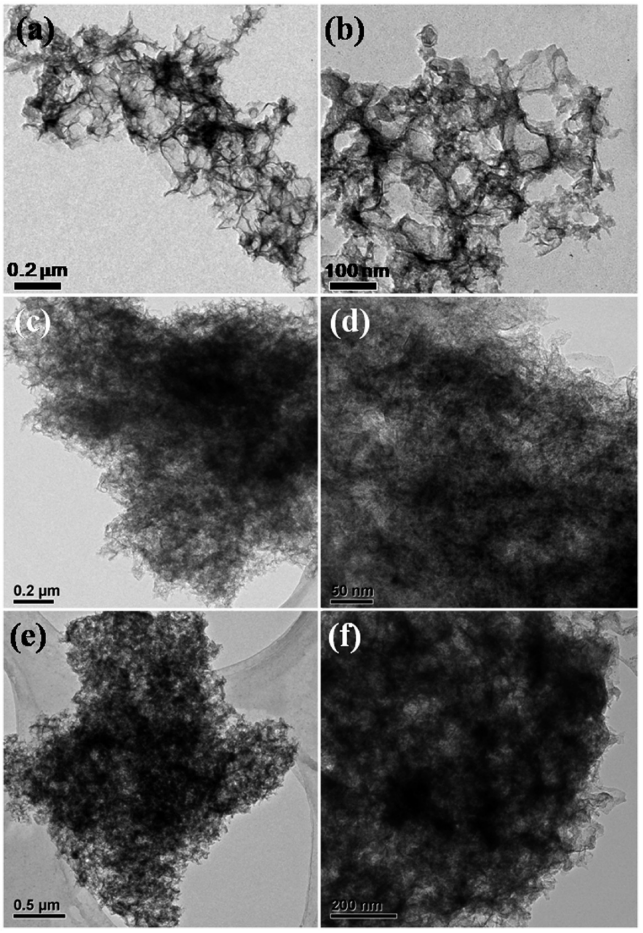

Figure 4. Low- and high-magnification TEM images of (a, b) porous graphitic carbon, (c, d) 60.8%S/PC, and (e, f) 88.9%S/PC.

60.8%S/PC, and we cannot observe large sulfur particles. However, we can clearly observe part of the aggregated sulfur particles on the surface of porous graphitic carbon in the TEM images of 88.9%S/PC (Figure 4e, f) even most of the sulfur nanoparticles are uniformly distributed, which should be owing to the limitation of pore volume of porous graphitic carbon. This is in agreement with the result reported by Gao et al.[39] and most of the previous reported results concerning sulfur/carbon composites with high sulfur loading.[3] We have further used TEM elemental mapping to compare the morphology difference between 60.8%S/PC and 88.9%S/PC. In the case of 60.8%S/PC, carbon (Figure 5b) and sulfur (Figure 5c) elementals both show homogenous distribution, demonstrating that the sulfur nanoparticles are homogeneously dispersed into the porous graphitic carbon matrix, and we cannot clearly observe large aggregated sulfur particles in the HAADF-STEM image of 60.8%S/PC (Figure 5a). On the other hand, the carbon (Figure 5e) and sulfur (Figure 5f) elementals mapping suggest the presence of part of aggregated sulfur particles in the 88.9%S/PC. From the HAADF-STEM image of 88.9%S/PC (Figure 5d), we can clearly observe aggregation of sulfur on the surface of porous graphitic carbon matrix, which is in agreement with the analysis results of XRD, SEM and TEM.

The electrochemical properties of 60.8%S/PC-AB, 88.9%S/PC-AB and S-AB electrodes using conventional acetylene black (AB) as conductive agent are evaluated by assembling them into coin cells with lithium as reference and counter electrode, 1.0 M lithium bis-trifluoromethanesulfonylimide in a mixture of 1,3-dioxolane (DOL) and dimethoxyethane (DME) (1:1 by volume) with 0.2 M $LiNO_3$ additive as electrolyte. Figure 6a and Figure 6b show the cyclic voltammograms (CVs) of 60.8% S/PC-AB and 88.9%S/PC-AB electrodes, respectively. For the 60.8%S/PC-AB electrode, during the first cathodic scan, three main peaks appear at ca. 2.30, 2.03, and 1.72 V, respectively. According to our previous reported results[3,4,34] and other works concerning Li−S batteries,[15,20,22] the peak at 2.30 V can be assigned to the reduction of sulfur to dissolved long-chain lithium polysulfides (Li_2S_x, $4 \leq x \leq 8$), see eqs 1, 2, and 3 below. The peak at 2.03 V corresponds to the reduction of long-chain polysulfides to short-chain polysulfides, see eqs 4

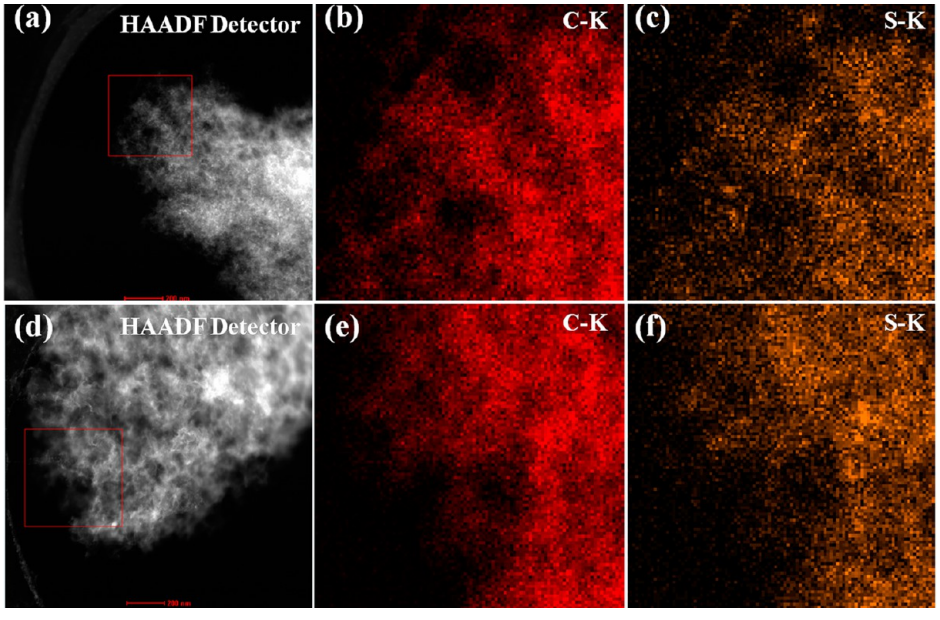

Figure 5. HAADF-STEM images and corresponding elementals mapping of carbon and sulfur across the selected areas (red square in the STEM) of (a−c) 60.8%S/PC and (d− f) 88.9%S/PC.

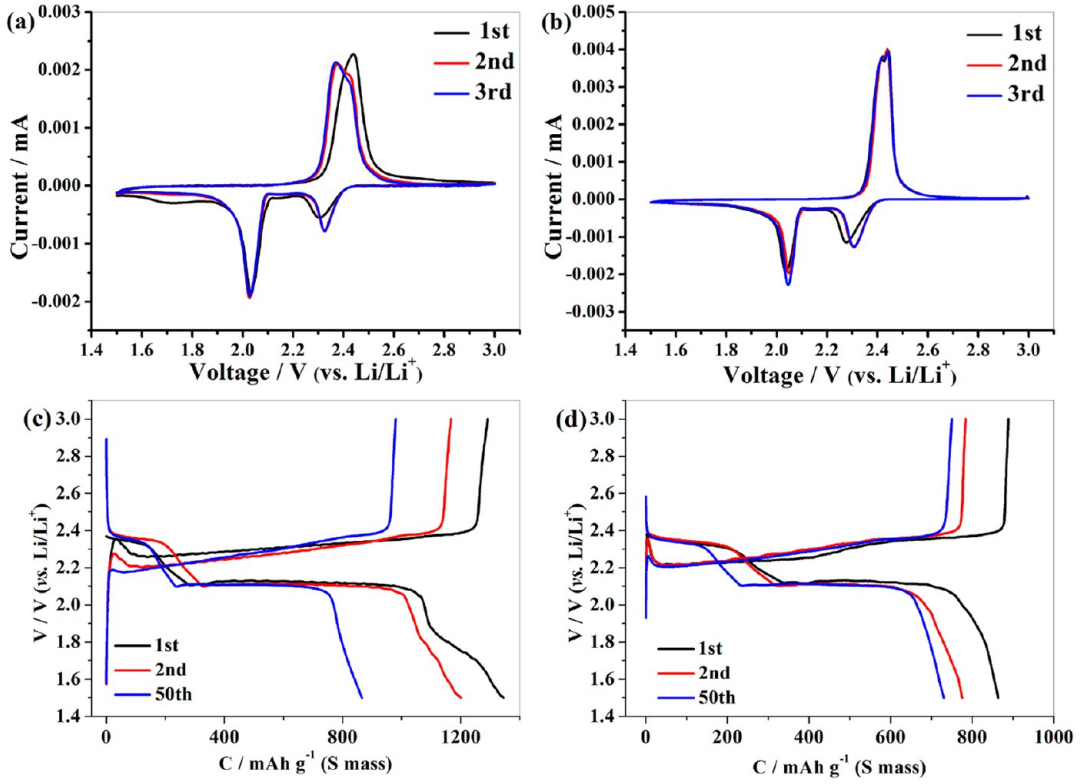

Figure 6. Cyclic voltammograms of the (a) 60.8%S/PC-AB and (b) 88.9%S/PC-AB electrodes at a scan rate of 0.1 mV s^{-1}; 1st, 2nd, and 50th charge/discharge curves of (c) 60.8%S/PC-AB and (d) 88.9%S/PC-AB electrodes at 0.1C.

and 5 below. The weak and broad peak appeared at 1.72 V is also reported by Zhang,[8,40] and is assigned to the reduction of $LiNO_3$. In order to confirm it, CV of porous carbon in the $LiNO_3$-contained electrolyte has been recorded (see Figure S3a in the Supporting Information). As shown, an initial reduction peak appears at around 1.6 V and becomes weaker in the subsequent cycles. We have further tested the CV of 60.8%S/PC electrode in the DOL-DME electrolyte without $LiNO_3$ additive (see Figure S3b in the Supporting Information). In this case, the initial reduction peak at 1.72 V cannot be observed. On the basis of the above two CV results, the initial reduction peak at 1.72 V should be associated with the decomposition of $LiNO_3$.

$$1/2S_8 + Li^+ + e^- \rightarrow 1/2Li_2S_8(1/4e^-, 209\ mAh\ g^{-1}{}_{(s)}) \quad (1)$$

$$3/2Li_2S_8 + Li^+ + e^- \rightarrow 2Li_2S_6(1/12e^-, 70\ mAh\ g^{-1}{}_{(s)}) \quad (2)$$

$$Li_2S_6 + Li^+ + e^- \rightarrow 3/2Li_2S_4(1/6e^-, 139\ mAh\ g^{-1}{}_{(s)}) \quad (3)$$

$$1/2Li_2S_4 + Li^+ + e^- \rightarrow Li_2S_2(1/2e^-, 418\ mAh\ g^{-1}{}_{(s)}) \quad (4)$$

$$1/2Li_2S_2 + Li^+ + e^- \rightarrow Li_2S(e^-, 836\ mAh\ g^{-1}{}_{(s)}) \quad (5)$$

In the anodic scan, only one oxidation peak at 2.44 V is observed, which is related to the conversion of Li_2S and/or short-chain polysulfides to long-chain polysulfides. In the subsequent scans, the reduction peak at 2.30 V is shifted to a slightly higher potential (2.33 V); the oxidation peak at 2.44 V becomes less significant and a new peak at 2.37 V grows higher in intensity, indicating an improvement of reversibility of the electrode with cycling.[15] In the case of the 88.9%S/PC-AB (Figure 6b) and S-AB (Figure S4a in Supporting Information) electrodes, most of the CV characteristics are similar to those of 60.8%S/PC-AB electrode except for the absence of the weak and broad reduction peak at 1.72 V.

Figure 6c illustrates the 1st, 2nd, and 50th charge/discharge curves of the 60.8%S/PC-AB electrode at 0.1 C. Two discharge plateaus at ca. 2.33 V and 2.10 V are observed, representing the two−step reaction process of sulfur with lithium in the discharge process. In addition, a small discharge plateau from 1.88 to 1.70 V in the 1st cycle can be observed, corresponding to the reduction peak at 1.72 V in the CV of 60.8%S/PC-AB. During its charge process, there is a long charge plateau ranging from 2.26 to 2.40 V, ascribing to the transformation of Li_2S_2 or Li_2S to long-chain polysulfides as mentioned above. In the case of the 88.9%S/PC-AB electrode (Figure 6d), the discharge plateau from 1.88 to 1.7 V in the 1st cycle is invisible, which exhibits an inclined line and is similar to most of the charge/discharge profiles for sulfur-based electrodes in Li−S batteries.[3,4,34] The initial discharge specific capacity (DC) of 60.8%S/PC-AB is measured as high as 1345.5 mAh $g^{-1}{}_{(S)}$, representing a high sulfur utilization of 80.0%. In addition, the initial charge specific capacity is 1291.6 mAh $g^{-1}{}_{(S)}$, resulting in a coulombic efficiency (CE = discharge capacity/charge capacity) of 104.2%. For the 88.9%S/PC-AB electrode, the initial discharge and charge specific capacities are 863.6 and 888.6 mAh $g^{-1}{}_{(S)}$, respectively, corresponding to an initial CE of 97.2%. The fact that the 88.9%S/PC-AB delivers a lower discharge specific capacity than 60.8%S/PC-AB should be attributed to the higher sulfur loading in the 88.9%S/PC, which will decrease the conductivity of the sulfur/porous graphitic

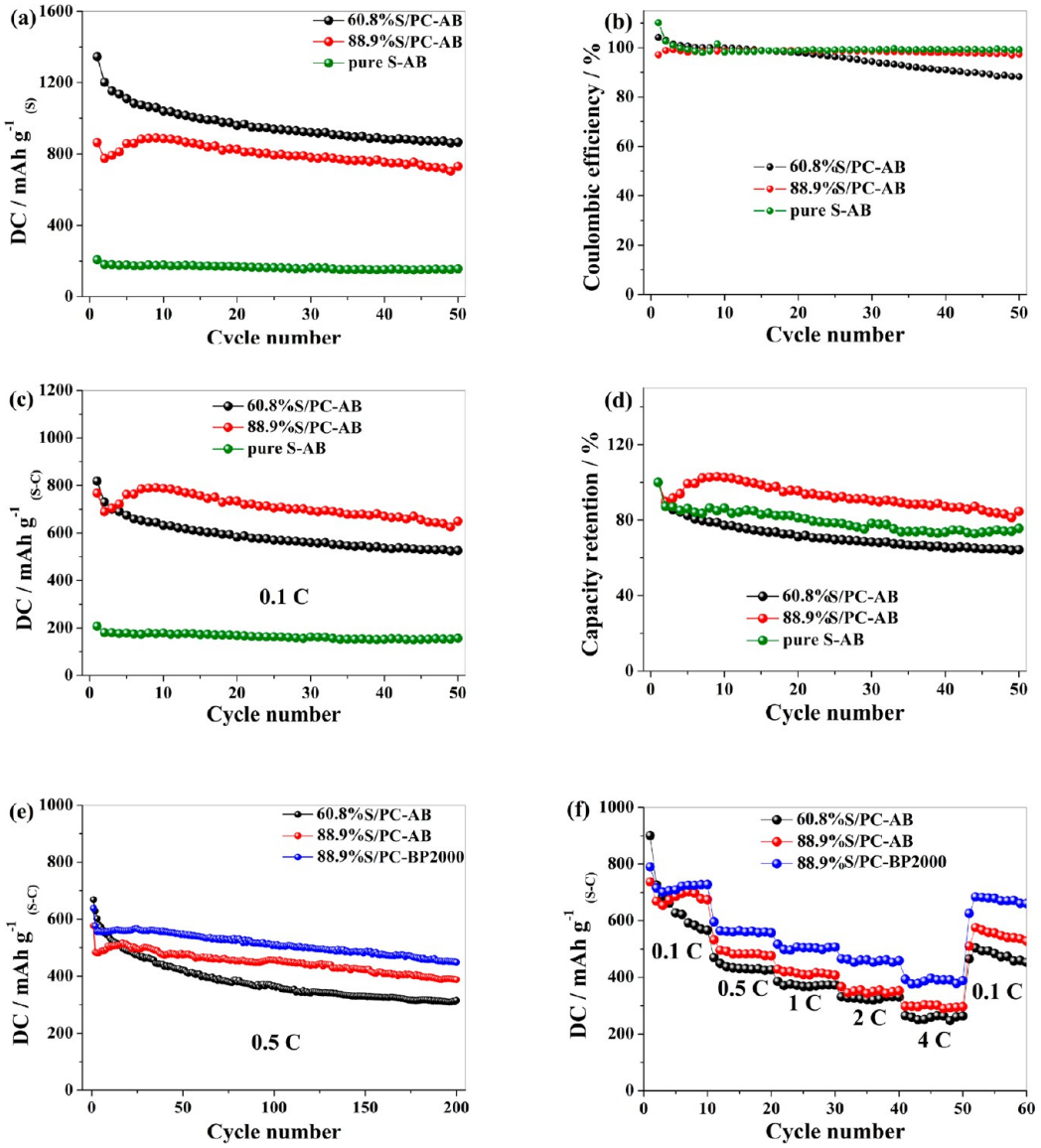

Figure 7. (a) Discharge specific capacities, (b) Coulombic efficiency, (c) overall discharge capacities, and (d) capacity retention of S-AB, 60.8%S/PC-AB and 88.9%S/PC-AB electrodes verse cycle number at 0.1C; (e) overall discharge capacities verse cycle number at 0.5C; and (f) rate capability of 60.8%S/PC-AB, 88.9%S/PC-AB, and 88.9%S/PC-BP2000 electrodes.

carbon composite and lower the electrochemical contact with sulfur. For the S-AB electrode (see Figure S4b in the Supporting Information), it exhibits quite a large voltage polarization and low charge/discharge specific capacities, which should be ascribed to its large sulfur particle size and poor electronic conductivity.

Figure 7a compares the discharge capacity variations of 60.8%S/PC-AB, 88.9%S/PC-AB, and S-AB electrodes along with increasing cycle number at a rate of 0.1 C. The 60.8%S/PC-AB could maintain a high discharge specific capacity of 865.3 mAh $g^{-1}_{(S)}$ after 50 cycles, which is very close to our previous reported data for S/(rGO, OMC, EG) composites[3,4,34] and sulfur/carbon composites with similar sulfur loading.[27,33] In the case of the 88.9%S/PC-AB electrode, the discharge specific capacity at the 50th cycle is slightly lower, i.e., 730.5 mAh $g^{-1}_{(S)}$. However, for the S-AB electrode, it can only deliver a discharge specific capacity of 156.5 mAh $g^{-1}_{(S)}$ after 50 cycles, indicating a much lower discharge specific capacity than 60.8%S/PC-AB and 88.9%S/PC-AB electrodes. The result demonstrates that by encapsulation of sulfur nanoparticles into the as-prepared porous graphitic carbon matrix, it can efficiently improve the sulfur utilization and charge/discharge specific capacity. In Figure 7b the CE of 60.8%S/PC, 88.9%S/PC, and S-AB electrodes at 0.1 C in the DOL-DME electrolyte with 0.2 M $LiNO_3$ as additive are also compared. It is known that the $LiNO_3$ can passivate the surface of lithium anode and thus reduce the polysulfides shuttle effect.[41] However, it obviously demonstrates that the CE of the 60.8%S/PC-AB electrode after 50 cycles is only 88.3%, in comparison with 97.4% for 88.9%S/PC-AB electrode and 99.2% for S-AB electrode. The result indicates that the polysulfide shuttle phenomenon in the 88.9% S/PC-AB and S-AB electrodes has been well reduced by adding $LiNO_3$ additive in the ether-based electrolyte. However, for the 60.8%S/PC-AB electrode, it displays a continuous CE fading in 50 cycles, illustrating an aggravated polysulfide shuttle phenomenon. The reason for such difference amongst the three electrodes will be discussed below.

It is worthwhile pointing out that most of carbon materials can only offer little capacity in the tested voltage range of sulfur-based electrodes. Therefore, the content of sulfur loading has a great influence on the overall capacity of sulfur/carbon composites, and further the energy density of Li−S cell. Considering a practical application, we measure the overall capacities of sulfur/porous graphitic carbon composites. The overall discharge capacities of 60.8%S/PC-AB, 88.9%S/PC-AB, and S-AB electrodes calculated based on the mass of sulfur/porous graphitic carbon composites are compared in Figure 7c. It clearly shows that the 88.9%S/PC-AB electrode can maintain higher overall discharge capacity of 649.4 mAh $g^{-1}_{(S-C)}$ after 50 cycles at 0.1*C* than the S-AB and 60.8%S/PC-AB electrodes. This should be ascribed to its remarkable discharge specific capacity with such a high sulfur loading. It is known that the physical property (e.g., electronic conductivity, pore volume, specific surface area...) of carbon material greatly affects the electrochemical performance of sulfur/carbon composites.[4,42−46] In the previous reported results, sulfur/carbon composites with high sulfur loading (>80 wt %) cannot maintain both a high specific capacity and a good cycleability.[34,36] The excellent electrochemical property of the 88.9%S/PC-AB could be attributed to characters of the as-prepared porous graphitic carbon such as high specific surface area, high pore volume and high electronic conductivity that originated from increase graphitization. However, because of the low tap density of the as-prepared porous graphitic carbon, it is difficult to measure directly its electronic conductivity. Therefore, the electrochemical impedance spectroscopy (EIS) is used to determine the electronic conductivity. As demonstrated in Figure S5a in the Supporting Information, the intercept at the real axis Z' is assigned to the contact resistance (R1) at the active material/current collector interface, the ionic resistance of electrolyte and the intrinsic resistance of the active material. The semicircle in intermediate-frequency region is related to the charge transfer impedance (R2) on the electrode/electrolyte interface, and the inclined line in the low frequency region corresponds to the lithium diffusion process within electrodes. The difference of R1 between 60.8%S/PC-AB and 88.9%S/PC-AB electrodes may be due to the distance difference between sulfur cathode and Li anode in two cells. The contact resistance (R1) and charge transfer resistance (R2) of the 60.8%S/PC are determined as 3.8 and 18.2 Ω, whereas those of the 88.9%S/PC are 13.0 and 31.4 Ω, respectively. The result demonstrates that with the increase of sulfur loading, the contact and charge transfer resistance are both increased, resulting in the lower discharge specific capacity of 88.9%S/PC-AB than 60.8%S/PC-AB. As the amount of the conductive agent in the electrode has a great influence on the charge transfer resistance, we compare the charge transfer resistance of 60.8%S/PC-AB and 88.9%S/PC-AB with the values of sulfur/carbon composites using the same amount of conductive agent in the preparation of electrodes that reported in the literatures (see Table S1 in the Supporting Information).[10,11,13,34] The lower charge transfer resistance of 60.8%S/PC-AB and 88.9%S/PC-AB than the values reported in the literatures imply the good electronic conductivity of the as-prepared porous graphitic carbon. The result suggests the importance of the high electronic conductivity of carbon matrix on the electrochemical properties of sulfur/carbon composites with high sulfur loading. We have also tested the electrochemical impedance spectra of two S/PC electrodes after 200 cycles of charge/discharge at 0.5*C* (see Figure S5b in Supporting Information). As shown, there are two semicircles in these plots as can be clearly observed in the magnified image in the inset to Figure S5b of Supporting Information. This is similar to the results reported by Manthiram et al.[46,47] and Wang et al.[48] The semicircle at the high frequency is accordingly assigned to the resistance of surface layer formed on the sulfur/porous graphitic carbon cathode and lithium anode, the semicircle at the high-medium frequency is ascribed to the electrochemical charge transfer resistance. As illustrated by Figure S5b and its inset in the Supporting Information, the resistance of surface layer for 60.8%S/PC-AB is higher than that of 88.9%S/PC-AB. The reason will be given below. On the other hand, both the electrochemical transfer resistance for 60.8%S/PC-AB and 88.9%S/PC-AB after 200 cycles of charge/discharge is smaller than that before cycling. Such phenomenon can be also observed in other literatures reported concerning Li−S battery,[10,11,46−48] revealing that the surface electrochemical activity of the cathode is initiated by the charge/discharge process. Besides, the ultralow charge transfer resistances indicate that the high electronic conductivity of porous graphitic carbon can facilitate the lithium and electron transport during charge/discharge.

Figure 7d compares the capacity retentions of the three electrodes. It is interesting that the 88.9%S/PC-AB and S-AB electrode both presents higher capacity retention than 60.8%S/PC-AB electrode that have sulfur uniformly distributed into the porous graphitic carbon matrix after 50 cycles of charge/discharge at 0.1*C*. Sulfur/carbon composites can actually show stable cycling performance although amount of sulfur particles are found to be located on the carbon surface instead of within the pores as reported by Gao et al.[39] and Amine et al.[49] The reason for the lower capacity retention of 60.8%S/PC-AB should be partially ascribed to the much higher initial discharge specific capacity of 60.8%S/PC-AB than 88.9%S/PC-AB. Even the capacity retention of 60.8%S/PC-AB is lower than that of 88.9%S/PC-AB; the discharge specific capacity of 60.8%S/PC-AB after 50 cycles of charge/discharge is still higher than those of 88.9%S/PC-AB and S-AB electrodes. This should be ascribed to the higher electronic conductivity of 60.8%S/PC and well dispersion of sulfur nanoparticles in the porous graphitic carbon matrix. On the other hand, as reported by Wang et al., the sulfur/carbon ratio plays a great role on the cycleability of Li−S battery.[50] Although sulfur/carbon ratios in the sulfur/porous graphitic carbon composites in our study have affected their sulfur particle sizes. Therefore, the difference on the capacity retention amongst the three electrodes may be associated their sulfur particle sizes. Further discussion will be made below. Long cycleability of the 60.8%S/PC-AB and 88.9%S/PC-AB electrodes at a higher rate of 0.5*C* are compared in Figure 7e. We do not investigate the high rate property of S-AB electrode considering its poor electrochemical performance at 0.1*C*. Despite a lower overall discharge capacity than 60.8%S/PC-AB in the initial 10 cycles, the 88.9%S/PC-AB could deliver a higher overall discharge capacity of 387.9 mAh $g^{-1}_{(S-C)}$ after 200 cycles at 0.5 C, illustrating a good long cycleability. The overall discharge capacities of 60.8%S/PC-AB and 88.9%S/PC-AB at different rates are shown in Figure 7f. It can be found that the 88.9%S/PC could deliver higher discharge capacity than 60.8%S/PC at rates of 0.1, 0.5, and 1*C*. However, their overall discharge capacities at higher rates of 2 and 4*C* are very close, which may be related to the higher requirement on electronic conductivity of sulfur/carbon cathodes at high rates.

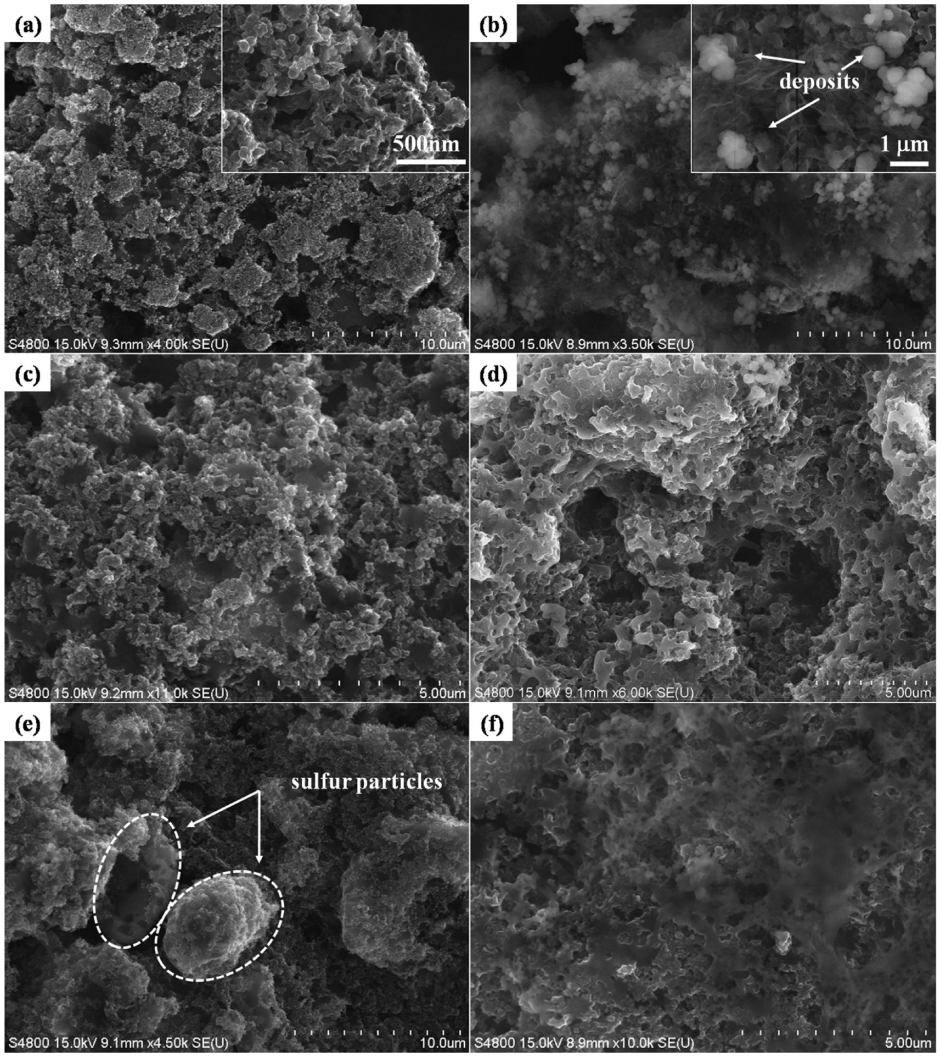

Figure 8. SEM images of the sulfur electrodes before and after 50 cycles of charge/discharge: 60.8%S/PC-AB electrode (a) before and (b) after; 88.9%S/PC-AB electrode: (c) before and (d) after; S-AB electrode: (e) before and (f) after.

In the current work, we further focus on study of conductive agent in preparation of electrodes. A well-known carbon material, i.e., BP2000 is served as conductive agent to replace conventional acetylene black during the preparation of 88.9%S/PC (88.9%S/PC-BP2000). As illustrated in Figure 7e, the overall discharge capacity of the 88.9%S/PC-BP2000 has been increased significantly by using BP2000 conductive agent, which can maintain a higher overall discharge capacity of 448.6 mAh $g^{-1}_{(S-C)}$ after 200 cycles at 0.5 C. It also shows an enhanced rate capability especially at high rates, as can be clearly observed in Figure 7f. The average overall discharge capacities of the 88.9%S/PC-BP2000 at rates of 0.1, 0.5, 1, and 2*C* are 725.0, 564.6, 504.2, and 459.0 mAh $g^{-1}_{(S-C)}$, respectively. At a high rate of 4 C, it can still release an overall discharge capacity of 387.2 mAh $g^{-1}_{(S-C)}$, which corresponds to a high specific capacity of 645.3 mAh $g^{-1}_{(S)}$ for sulfur/carbon composite with sulfur loading of 60 wt %, 774.4 mAh $g^{-1}_{(S)}$ for sulfur/carbon composite with sulfur loading of 50 wt % and 968 mAh $g^{-1}_{(S)}$ for sulfur/carbon composite with sulfur loading of 40 wt % at 4 C, illustrating excellent high rate property. When the rate is decreased to 0.1*C*, an average discharge capacity of 668.6 mAh $g^{-1}_{(S-C)}$ that is 92.2% of its initial average discharge capacity at 0.1*C* could be recovered. The improved performance of 88.9%S/PC using BP2000 instead of acetylene black as conductive agent should be attributed to the spherical morphology of BP2000, which is composed of chain-like interlaced nanoparticles (see Figure S6a in the Supporting Information). Such structural characteristic is beneficial for ensuring good conductivity of the BP2000. In contrast, the acetylene black nanoparticles are irregular and disorderly dispersed (Figure S6b in the Supporting Information). Li et al. have investigated the effect of matrix carbon materials influence on the performance of Li−S battery, and found that the sulfur/BP2000 composite can deliver much higher specific capacity and better cycle performance than sulfur/acetylene black composite.[51]

Figure 8 compares the morphology changes of 60.8%S/PC-AB, 88.0%S/PC-AB, and S-AB electrodes before and after 50 cycles of charge/discharge at 0.1 C. In the case of 60.8%S/PC-AB electrode, before charge/discharge (Figure 8a and the inset), no big sulfur particles could be observed, sulfur nanoparticles are uniformly distributed into the porous graphitic carbon matrix; while after 50 cycles of charge/discharge, lots of deposit-like particles around sub-micrometer form in high yield (Figure 8b), which may lead to the larger surface layer resistance of 60.8%S/PC-AB than 88.9%S/PC-AB

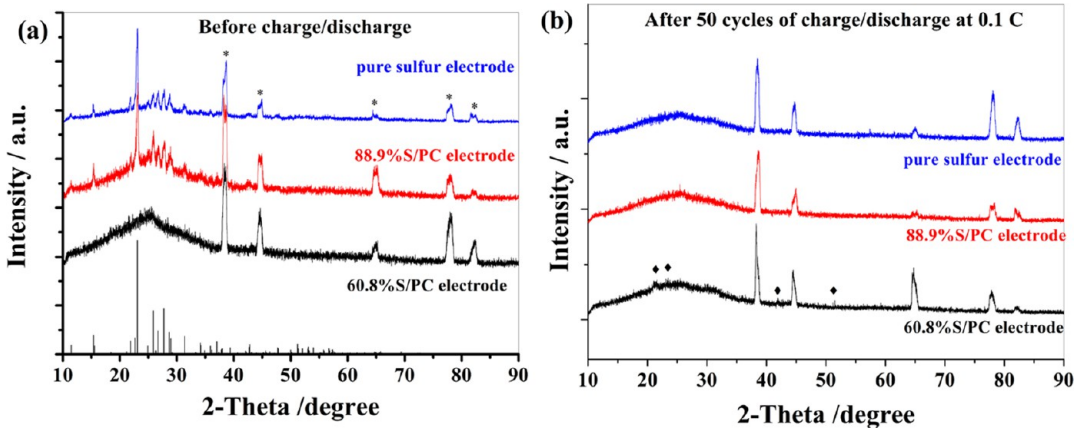

Figure 9. XRD patterns of S-AB, 60.8%S/PC-AB and 88.9%S/PC-AB electrodes: (a) before and (b) after 50 cycles of charge/discharge at 0.1C.

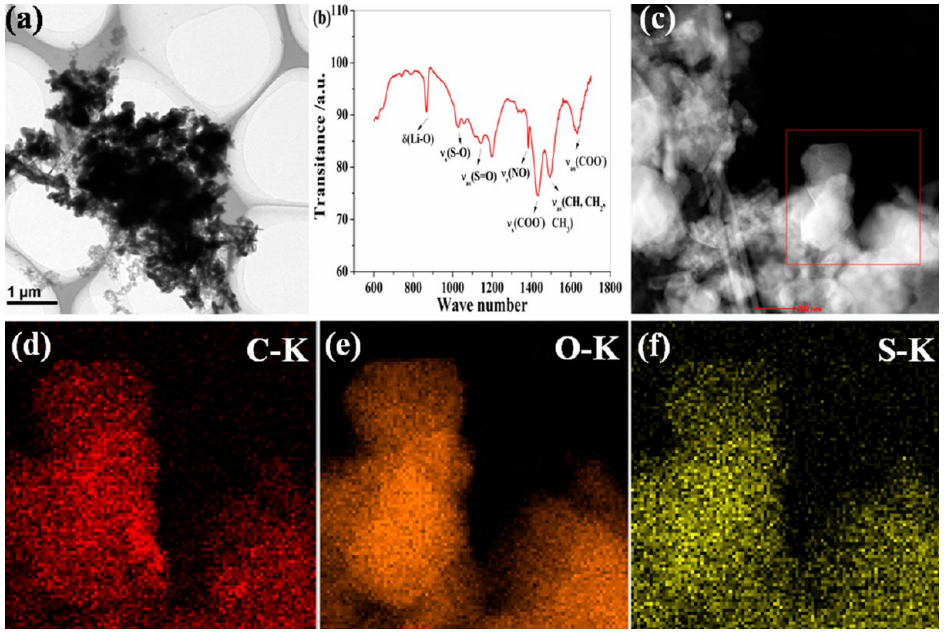

Figure 10. (a) TEM image, (b) FTIR spectrum, and (c) HAADF-STEM image and corresponding elementals mapping of (d) carbon, (e) oxygen, and (f) sulfur across a selected area (red square in the STEM) of 60.8%S/PC-AB electrode after 50 cycles of charge/discharge at 0.1C.

electrode after cycling. For the 88.9%S/PC-AB and S-AB electrodes, before charge/discharge (Figure 8c, e), their morphologies are quite similar with the SEM images of their raw materials. On the contrary, after 50 cycles of charge/discharge, the sulfur nanoparticles are disappeared and the deposit-like particles can be hardly seen (Figure 8d, f). Ex situ XRD is further used to characterize the composition variations of 60.8%S/PC-AB, 88.0%S/PC-AB, and S-AB electrodes before charge/discharge and after 50 cycles of charge/discharge at 0.1C (Figure 9). The strong diffraction peaks marked by asterisks at around 39.0, 44.7, 64.6, 78.1, and 82.0° in the Figure 9a are ascribed to the Al current collector. Before charge/discharge, in the case of 60.8%S/PC-AB electrode, no sulfur diffraction peaks could be observed, whereas for 88.9%S/PC-AB and S-AB electrodes, we can see sulfur diffraction peaks with strong intensity. These characteristics are all in accordance with XRD patterns of their raw materials (Figure 3). However, after 50 cycles of charge/discharge at 0.1 C, the strong sulfur diffraction peaks before charge/discharge have disappeared in the case of S-AB and 88.9%S/PC-AB electrodes. A broad amorphous peak range from 10 to 35° could be observed, indicating there are no big particles in the sublimed sulfur and 88.9%S/PC electrodes after charge/discharge. In contrast, for 60.8%S/PC-AB electrode, except the strong Al substrate diffraction peaks, we can see some diffraction peaks marked by diamond symbol. These peaks may come from the deposit-like particles formed after charge/discharge.

We have made accordingly additional analysis on the component of the solid deposits formed after charge/discharge in the 60.8%S/PC-AB electrode by TEM elemental mapping and FTIR analysis (Figure 10). Figure 10a shows the TEM image of 60.8%S/PC-AB electrode after 50 cycles of charge/discharge at 0.1C. In agreement with the SEM image of 60.8% S/PC-AB electrode after 50 cycles (Figure 8b), lots of large deposit-like particles are located on the surface of porous graphitic carbon. Such deposits have been also reported by Diao et al.,[52] we have done the FTIR analysis on the 60.8%S/PC-AB electrode after cycling as they have done. As shown in Figure 10b, the FTIR spectrum is very similar to the result reported by Diao et al., indicating the formation of HCO_2Li,

ROLi and Li_xSO_y species. As they reported, these species are electrolyte degradation products during charge/discharge, and they could co-deposit with Li_2S and Li_2S_2 in cathode, leading to formation of deposit-like particles and the capacity fading of 60.8%S/PC-AB. We further used TEM elemental mapping to investigate the component of the cycled 60.8%S/PC-AB electrode. As shown in Figure 10d−f, carbon, oxygen and sulfur elementals are uniformly distributed in the selected area by red square in the STEM image (Figure 10c), proving the formation of HCO_2Li, ROLi, and Li_xSO_y species (Noted that lithium is unable to be detected by TEM). The FTIR and TEM results demonstrate that, during charge/discharge, the electrolyte degradation for the 60.8%S/PC-AB is quite serious, leading to the formation of large deposit-like particles and decay of specific capacity and coulombic efficiency. While in the case of 88.9%S/PC-AB and S-AB electrode, as shown in images d and f in Figure 8, the large deposit-like particles could not be observed, resulting in their higher capacity retention and coulombic efficiency. Such difference may be attributed to their different sulfur particle sizes. The nano-sized sulfur in the 60.8% S/PC-AB has higher surface area and better contact with the electrolyte, which may lead to the serious electrolyte degradation as proved by FTIR and TEM. Therefore, owing to different sulfur particle sizes amongst sublimed sulfur, 60.8% S/PC, and 88.9%S/PC, they show different capacity retention, coulombic efficiency, and specific capacity.

4. CONCLUSIONS

In summary, a porous graphitic carbon is prepared by using commercial $CaCO_3$ nanoparticles as template and sucrose as carbon source followed by high temperature calcination. The BET result illustrates that the as-prepared porous graphitic carbon possess a porous structure with a high specific surface area of 1416 $m^2\ g^{-1}$ and a high pore volume of 1.11 $cm^3\ g^{-1}$ together with high electronic conductivity that is originated from increased graphitization. Sulfur/porous graphitic carbon composites with ultra high sulfur loading of 88.9 wt % and lower sulfur loading of 60.8 wt % are synthesized by a simple melt-diffusion strategy, and served as cathode for Li−S batteries. The electrochemical test results demonstrate that, in comparison with the 60.8%S/PC, the 88.9%S/PC illustrate higher overall discharge capacity, higher capacity retention and better coulombic efficiency after 50 cycles at a rate of 0.1−. It has also demonstrated that using BP2000 to replace conventional acetylene black as conductive agent can further improve the high rate property of 88.9%S/PC. The excellent electrochemical performance of 88.9%S/PC is attributed to the porous structure, high specific surface area, high pore volume, and high electronic conductivity of the porous graphitic carbon, which can provide stable electronic and ionic transfer channel.

■ ASSOCIATED CONTENT

Ⓢ Supporting Information

SEM images of 88.9%S/PC and sublimed sulfur. N_2 isotherm adsorption and desorption curves of porous graphitic carbon, 60.8%S/PC, 88.9%S/PC and sublimed sulfur. CV of porous carbon electrode in the $LiNO_3$-contained electrolyte and CV of 60.8%S/PC electrode in the DOL-DME electrolyte without $LiNO_3$, scan rates are both 0.1 mV s^{-1}. CV of S-AB electrode at a scan rate of 0.1 mV s^{-1} and charge/discharge curves of S-AB electrode at a rate of 0.1 C. Nyquist plots of 60.8%S/PC-AB and 88.9%S/PC-AB electrodes before and after 200 cycles of charge/discharge at 0.5 C. SEM images of BP2000 and acetylene black conductive agent. Comparison of charge transfer resistance and electrochemical performance of sulfur/porous graphitic carbon composites with those reported in the literature. This material is available free of charge via the Internet at http://pubs.acs.org/.

■ AUTHOR INFORMATION

Corresponding Author

*E-mail: sgsun@xmu.edu.cn.

Notes

The authors declare no competing financial interest.

■ ACKNOWLEDGMENTS

This work is supported by the Special Funds for Major State Basic Research Project of China (2009CB220102, 2011AA11A254) and NSFC (21021002).

■ REFERENCES

(1) Ji, X. L.; Lee, K. T.; Nazar, L. F. *Nat. Mater.* **2009**, *8*, 500−506.
(2) Liang, C. D.; Dudney, N. J.; Howe, J. Y. *Chem. Mater.* **2009**, *21*, 4724−4730.
(3) Sun, H.; Xu, G. L.; Xu, Y. F.; Sun, S. G.; Zhang, X. F.; Qiu, Y. C.; Yang, S. H. *Nano Res.* **2012**, *5*, 726−738.
(4) Chen, S. R.; Zhai, Y. P.; Xu, G. L.; Jiang, Y. X.; Zhao, D. Y.; Li, J. T.; Huang, L.; Sun, S. G. *Electrochim. Acta* **2011**, *56*, 9549−9555.
(5) Wang, J. L.; Yang, J.; Xie, J. Y.; Xu, N. X.; Li, Y. *Electrochem. Commun.* **2002**, *4*, 499−502.
(6) He, X. M.; Shi, Q.; Zhou, X.; Wan, C. R.; Jiang, C. Y. *Electrochim. Acta* **2005**, *51*, 1069−1075.
(7) Lee, Y. M.; Choi, N. S.; Park, J. H.; Park, J. K. *J. Power Sources* **2003**, *119*, 964−972.
(8) Zhang, S. S. *Electrochim. Acta* **2012**, *70*, 344−348.
(9) Hassoun, J.; Scrosati, B. *Adv. Mater.* **2010**, *22*, 5198−+.
(10) Li, G. C.; Li, G. R.; Ye, S. H.; Gao, X. P. *Adv. Energy Mater.* **2012**, *2*, 1238−1245.
(11) Fu, Y. Z.; Manthiram, A. *Rsc Adv.* **2012**, *2*, 5927−5929.
(12) Yang, Y.; Yu, G. H.; Cha, J. J.; Wu, H.; Vosgueritchian, M.; Yao, Y.; Bao, Z. A.; Cui, Y. *Acs Nano* **2011**, *5*, 9187−9193.
(13) Wu, F.; Chen, J. Z.; Chen, R. J.; Wu, S. X.; Li, L.; Chen, S.; Zhao, T. *J. Phys. Chem. C* **2011**, *115*, 6057−6063.
(14) Fanous, J.; Wegner, M.; Grimminger, J.; Andresen, A.; Buchmeiser, M. R. *Chem. Mater.* **2011**, *23*, 5024−5028.
(15) Zhou, G. M.; Wang, D. W.; Li, F.; Hou, P. X.; Yin, L. C.; Liu, C.; Lu, G. Q.; Gentle, I. R.; Cheng, H. M. *Energy Environ. Sci.* **2012**, *5*, 8901−8906.
(16) Dorfler, S.; Hagen, M.; Althues, H.; Tubke, J.; Kaskel, S.; Hoffmann, M. J. *Chem. Commun.* **2012**, *48*, 4097−4099.
(17) Wei, W.; Wang, J. L.; Zhou, L. J.; Yang, J.; Schumann, B.; NuLi, Y. N. *Electrochem. Commun.* **2011**, *13*, 399−402.
(18) Guo, J. C.; Xu, Y. H.; Wang, C. S. *Nano Lett.* **2011**, *11*, 4288−4294.
(19) Ahn, W.; Kim, K. B.; Jung, K. N.; Shin, K. H.; Jin, C. S. *J. Power Sources* **2012**, *202*, 394−399.
(20) Jayaprakash, N.; Shen, J.; Moganty, S. S.; Corona, A.; Archer, L. A. *Angew. Chem. Int. Ed.* **2011**, *50*, 5904−5908.
(21) Zhang, B.; Qin, X.; Li, G. R.; Gao, X. P. *Energy Environ. Sci.* **2010**, *3*, 1531−1537.
(22) Schuster, J.; He, G.; Mandlmeier, B.; Yim, T.; Lee, K. T.; Bein, T.; Nazar, L. F. *Angew. Chem., Int. Ed.* **2012**, *51*, 3591−3595.
(23) Ding, B.; Yuan, C. Z.; Shen, L. F.; Xu, G. Y.; Nie, P.; Zhang, X. G. *Chem-Eur. J.* **2013**, *19*, 1013−1019.
(24) Rao, M. M.; Song, X. Y.; Liao, H. G.; Cairns, E. J. *Electrochim. Acta* **2012**, *65*, 228−233.
(25) Ji, L. W.; Rao, M. M.; Aloni, S.; Wang, L.; Cairns, E. J.; Zhang, Y. G. *Energy Environ. Sci.* **2011**, *4*, 5053−5059.
(26) Zheng, G. Y.; Yang, Y.; Cha, J. J.; Hong, S. S.; Cui, Y. *Nano Lett.* **2011**, *11*, 4462−4467.

(27) Ji, L. W.; Rao, M. M.; Zheng, H. M.; Zhang, L.; Li, Y. C.; Duan, W. H.; Guo, J. H.; Cairns, E. J.; Zhang, Y. G. *J. Am. Chem. Soc.* **2011**, *133*, 18522−18525.
(28) Zhang, F. F.; Zhang, X. B.; Dong, Y. H.; Wang, L. M. *J. Mater. Chem.* **2012**, *22*, 11452−11454.
(29) Li, N. W.; Zheng, M. B.; Lu, H. L.; Hu, Z. B.; Shen, C. F.; Chang, X. F.; Ji, G. B.; Cao, J. M.; Shi, Y. *Chem. Commun.* **2012**, *48*, 4106−4108.
(30) Yin, L. C.; Wang, J. L.; Lin, F. J.; Yang, J.; Nuli, Y. *Energy Environ. Sci.* **2012**, *5*, 6966−6972.
(31) Wang, J. Z.; Lu, L.; Choucair, M.; Stride, J. A.; Xu, X.; Liu, H. K. *J. Power Sources* **2011**, *196*, 7030−7034.
(32) Wang, H. L.; Yang, Y.; Liang, Y. Y.; Robinson, J. T.; Li, Y. G.; Jackson, A.; Cui, Y.; Dai, H. J. *Nano Lett.* **2011**, *11*, 2644−2647.
(33) Cao, Y. L.; Li, X. L.; Aksay, I. A.; Lemmon, J.; Nie, Z. M.; Yang, Z. G.; Liu, J. *Phys. Chem. Chem.Phys.* **2011**, *13*, 7660−7665.
(34) Wang, Y. X.; Huang, L.; Sun, L. C.; Xie, S. Y.; Xu, G. L.; Chen, S. R.; Xu, Y. F.; Li, J. T.; Chou, S. L.; Dou, S. X.; Sun, S. G. *J. Mater. Chem.* **2012**, *22*, 4744−4750.
(35) Evers, S.; Nazar, L. F. *Chem. Commun.* **2012**, *48*, 1233−1235.
(36) Li, D.; Han, F.; Wang, S.; Cheng, F.; Sun, Q.; Li, W. C. *ACS Appl. Mater. Interfaces* **2013**, *5*, 2208−2213.
(37) Manthiram, A.; Fu, Y. Z.; Su, Y. S. *Acc. Chem. Res.* **2012**, *5*, 1125−1134.
(38) Liao, Y. P.; Pan, K.; Wang, L.; Pan, Q. J.; Zhou, W.; Miao, X. H.; Jiang, B. J.; Tian, C. G.; Tian, G. H.; Wang, G. F.; Fu, H. G. *ACS Appl. Mater. Interfaces* **2013**, *5*, 3663−3670.
(39) Li, G. C.; Hu, J. J.; Li, G. R.; Ye, S. H.; Gao, X. P. *J. Power Sources* **2013**, *240*, 598−605.
(40) Zhang, S. S. *J. Electrochem. Soc.* **2012**, *159*, A1226−A1229.
(41) Aurbach, D.; Pollak, E.; Elazari, R.; Salitra, G.; Kelley, C. S.; Affinito, J. *J. Electrochem. Soc.* **2009**, *156*, A694−A702.
(42) Li, X. L.; Cao, Y. L.; Qi, W.; Saraf, L. V.; Xiao, J.; Nie, Z. M.; Mietek, J.; Zhang, J. G.; Schwenzer, B.; Liu, J. *J. Mater. Chem.* **2011**, *21*, 16603−16610.
(43) Wei, S. C.; Zhang, H.; Huang, Y. Q.; Wang, W. K.; Xia, Y. Z.; Yu, Z. B. *Energy Environ. Sci* **2011**, *4*, 736−740.
(44) He, G.; Ji, X. L.; Nazar, L. *Energy Environ. Sci* **2011**, *4*, 2878−2883.
(45) Sun, F. G.; Wang, J. T.; Chen, H. C.; Li, W. C.; Qiao, W. M.; Long, D. H.; Ling, L. C. *ACS Appl. Mater. Interfaces* **2013**, *5*, 5630−5638.
(46) Fu, Y. Z.; Su, Y. S.; Manthiram, A. *ACS Appl. Mater. Interfaces* **2012**, *4*, 6046−6052.
(47) Fu, Y. Z.; Manthiram, A. *Chem. Mater.* **2012**, *24*, 3081−3087.
(48) Wang, B.; Li, K. F.; Su, D. W.; Ahn, H. J.; Wang, G. X. *Chem−Asian J.* **2012**, *7*, 1637−1643.
(49) Weng, W.; Pol, V.; Amine, K. *Adv. Mater.* **2013**, *25*, 1608−1615.
(50) Chen, S. R.; Dai, F.; Gordin, M.; Wang, D. H. *Rsc Adv.* **2013**, *3*, 3540.
(51) Li, C. L.; Shan, Z. Q.; Tian, J. H. *J. Funct. Mater.* **2012**, *43*, 880−883.
(52) Diao, Y.; Xie, K.; Xiong, S. C.; Hong, X. B. *J. Electrochem. Soc.* **2012**, *159*, A1816−A1821.